

# Experimental analysis and numerical simulation of sintered micro-fluidic devices

J.-C. Gelin<sup>1</sup>, M. Sahli<sup>1,2</sup>, T. Barrière<sup>1</sup>

1. Femto-st Institute/Applied Mechanics Department, 24 chemin de l'épitaphe, Besançon, France  
2. Mechanics Laboratory, Faculty of Engineering Sciences, University Mentouri, Constantine, Algeria

## Abstract:

*This paper investigates the use of numerical simulations to describe the solid state diffusion of a sintering stage during a powder hot embossing (PHE) process for micro-fluidic components. Finite element analysis based on a thermo-elasto-viscoplastic model was established to describe the densification process of a PHE stainless steel porous component during sintering. The numerical analyses, which were performed on a 3D micro-structured component, demonstrated that the FE simulation results are in better agreement with the experimental results at high temperatures.*

**Mots clefs : hot embossing, sintering, numerical simulation, constitutive equations, 316L stainless steel powders**

## 1 Introduction

The metal hot embossing (MHE) process has become a viable, low-cost process for producing parts with complex shapes in short series. MHE combines the shaping efficiency of polymer hot embossing with the capability of powder metallurgy [1-3], which offers many unique advantages in the production of near neat shape micro-structured components. This process is actually a multi-step process divided into compounding, hot embossing, debinding and sintering components [4,5]. The goal of mixing steps is to form the feedstock for hot embossing by mixing the metallic powders with thermoplastic binders. The binders used in hot embossing are commonly used polymer mixtures, such as polypropylene, a synthetic or natural wax and stearic acid. The resulting mixture is called a feedstock, which is then embossed in a mould to achieve the required shapes. Afterwards, the binder is removed during thermal debinding, and the powder is sintered, yielding the full density necessary to give the required mechanical properties and geometric size; at the same time, a certain amount of shrinkage occurs (see Fig. 1).

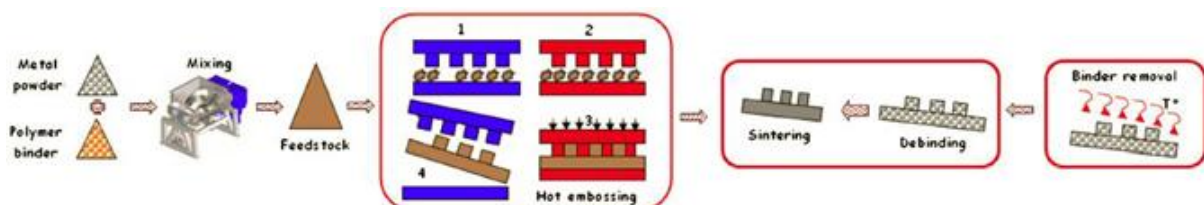


Fig. 1. Schematic illustration of the multi-stages sequential manufacturing process used for micro-structured mould inserts, which combines the hot embossing process and powder metallurgy processes.

The sintering stage can be defined as a thermal transformation of bulk materials into compact solids at temperatures below their melting point [6,7]. The primary phenomenon is solid state diffusion, which

occurs along the different interfaces of the crystals and through any vacancies. However, in the MHE process, the metallic components undergo contraction and deformation, leading to challenges in terms of determining the initial structure design of the die mould cavities, the initial size and the processing parameters. In this paper, the material and process sintering parameters are identified from dilatometer experimental data. The model and the identified material parameters are implemented in a finite element solver to perform the numerical simulation of the sintering step associated with MHE. Sintering experiments were performed in a batch furnace to verify the numerical model and simulations on 316L stainless steel.

## 2 Constitutive Equations for the Sintering Process

The proposed model is based on the assumption that a porous material follows a linear-viscous behaviour and behaves according to the continuum theory of sintering [8]. This model is a phenomenological model based on continuum mechanics and uses thermo-elasto-visco-plastic formulations, which are related by the following equation:

$$\dot{\varepsilon} = \dot{\varepsilon}_e + \dot{\varepsilon}_{th} + \dot{\varepsilon}_{vp} \Rightarrow \dot{\varepsilon} = C_e \dot{\sigma} + \alpha \Delta \dot{T} I + \frac{dev(\sigma)}{2G} + \frac{\sigma_m - \sigma_s}{3K} I \quad (1)$$

where  $C_e$  is the elastic compliance matrix,  $\Delta T$  is the incremental temperature rate,  $I$  is the second-order identity tensor,  $\alpha$  is the thermal expansion coefficient determined experimentally using a dilatometer,  $\sigma_m = tr(\sigma)/3$  is the trace of the stress tensor,  $G$  and  $K$  are the shear and bulk viscosity moduli, respectively, and  $\sigma_s$  is the sintering stress. The variables  $G$ ,  $K$  and  $\sigma_s$  are material parameters that still need to be determined. Song et al. (2006) derived the following relationship to define the uniaxial viscosity  $\eta_{ep}$  through bending tests in a dilatometer:

$$\eta_p^e = \frac{1}{\dot{\delta}} \left( \frac{5\rho_a g L_s^4}{32h^2} + \frac{P L_s^3}{4bh^3} \right) \quad (2)$$

where  $\delta$  is the deflection rate at the centre of the specimen,  $\rho_a$  is the apparent density,  $g$  is gravity,  $P$  is the external load, and  $L_s$ ,  $b$  and  $h$  are the distance between the two supporting rods and the width and thickness of the specimen. The following equation is used to determine the sintering stress:

$$\sigma_s = B \rho^C \quad (3)$$

where  $B$  and  $C$  are material parameters identified from dilatometry experiments. Using these proposed constitutive equations, the related material parameters can be determined.

The proper strategy consists of identifying parameters  $B$  and  $C$ , which determine the numerical shrinkage curve according to Eq. (4), in Matlab<sup>®</sup>. Therefore, the minimisation algorithm is used to, as best as possible, fit the simulations to the experimental curves by adjusting the physical parameters:

$$\begin{cases} \min F(x) \\ F(x) = \sum_{i=1}^n \left| \lambda^m(T_i, x) - \lambda^e(T_i, x) \right|^2 \\ x = [B, C] \end{cases} \quad (4)$$

where  $\lambda_e$  is the experimental uniaxial shrinkage obtained from the dilatometry tests,  $\lambda_m$  is the numerical uniaxial shrinkage.

## 3 Materials and Experimental Methods

### 3.1 Materials

In the present analysis, the stainless steel powders (Osprey<sup>®</sup> Sandvik, UK) used exhibit a particle size distribution as follows:  $d_{10}=1.8 \mu\text{m}$ ,  $d_{50}=3.5 \mu\text{m}$  and  $d_{90}=5.0 \mu\text{m}$  (see Fig. 2a). The binder system used

in this study consisted of paraffin wax (PW), polypropylene (PP) and stearic acid (SA), and the highest melting temperature of the binder system measured on a Setaram differential scanning calorimeter (DSC 92) is 160 °C. The composition of the binder, which corresponds to the ratio of PP/PW/SA, is given as the relative fraction 40/55/5. The characteristics of the different binder systems are presented in Table 1.

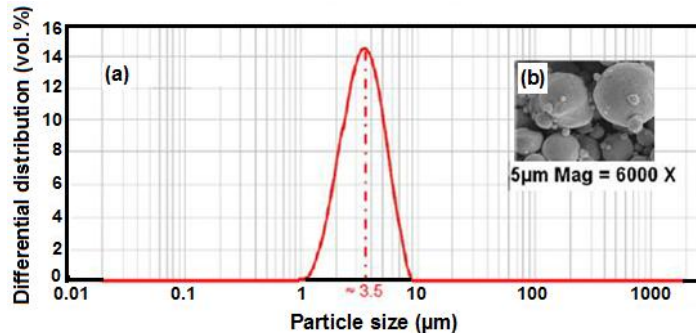


Fig. 2. (a) Particle size distribution and (b) SEM micrograph of the 316L stainless steel powder.

Experiments related to the mixing of binders and feedstocks were performed using a twin-screw Brabender<sup>®</sup> Plastograph EC mixer with a pair of rotor blades. The same processing conditions were used for each mixture, including a mixing temperature of 180 °C, a mixing time of 30 min and a mixing rotation speed of 30 rpm.

Table 1. Characteristics of the different binder components.

Binders	Density [g/cm <sup>3</sup> ]	Melting temperature [°C]
Stearic acid (SA)	0.89	70
Paraffin wax (PW)	0.91	60
Polypropylene (PP)	0.90	160

### 3.2 Identification of sintering parameters

The sintering experiments under argon atmosphere were performed in the vertical dilatometer to identify the sintering parameters of the model (see Fig. 3). For identical heating rates, the uniaxial viscosities are higher for a higher feedstock solid loading at the same temperature. Complementary tests were performed in a compression configuration using a vertical dilatometer. Shrinkage begins to occur at approximately 1000 °C and rapidly increases at temperatures greater than 1050 °C until approximately 1170 °C. At the same temperature, significant shrinkage is obtained for the specimens developed at a lower powder loading because when the powder loading is high, more pores are produced and the components shrink more obviously after sintering stage.

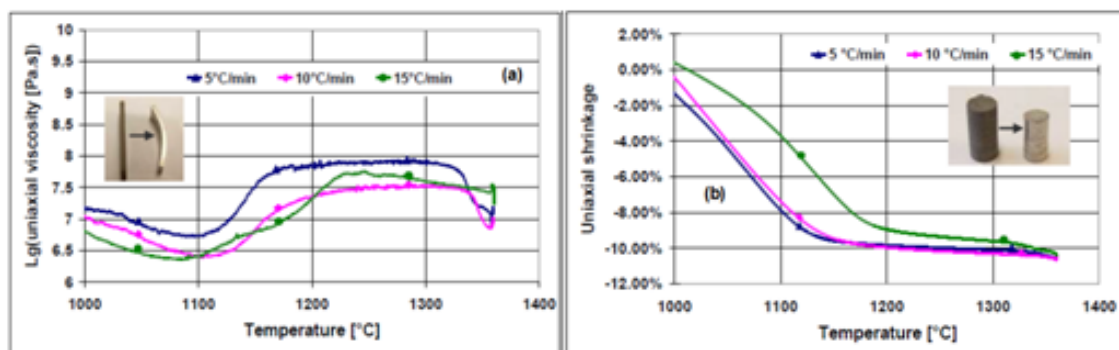


Fig. 3. Uniaxial viscosity vs. temperature from (a) beam-bending tests and (b) free-sintering tests conducted in a vertical dilatometer for 316L stainless steel feedstock.

## 4 Finite Element Model of the Sintering Process

### 4.1 Boundary and initial conditions

A micro-fluidic geometry with dimensions of 70x30x5 mm<sup>3</sup> and micrometric grounds on the order of 100 μm is shown in Fig. 4a. The element type and mesh are defined for the geometries as shown in Fig. 4b. The anisotropic mesh is composed of 33540 nodes and 19235 C3D8R elements, and the densification support used is composed of 1896 nodes and 1170 R3D4 elements. The plate support is assumed to be a rigid body during the simulation, and the micro-fluidic replicas follow thermo-elasto-viscoplastic behaviour.

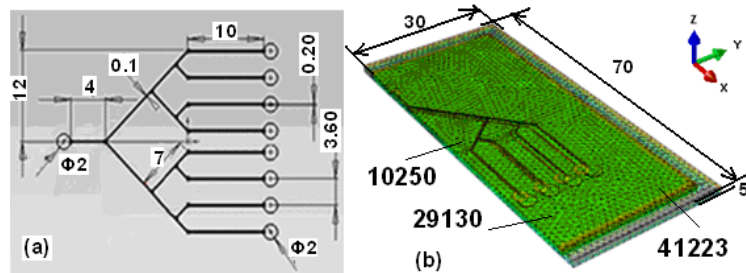


Fig. 4. (a) Geometry of micro-fluidic specimens. Dimensions of samples under sintered condition (units are in mm), (b) FE meshes of the micro-fluidic component and the plate support prior to the simultaneous sintering stages.

### 4.2 Numerical results and discussion

Simulation of the micro-fluidic replicas was performed with the ABAQUS<sup>®</sup> finite element solver based on the above models and identified parameters. Fig. 5a displays the relative density distribution contour after hot embossing, with its lowest value of 61.20% in the central area and highest value of 62.4% at the outside of the micro-fluidic component. In the powder hot embossing process, this segregation occurs between the powders and binders due to their different values of inertia. This induces inhomogeneous density distributions in the green parts. The relative density gap was broadened by ~4% during the hot embossing process and narrowed after sintering. This result also indicates that sintering assists in balancing the density distribution and narrowing the inhomogeneity.

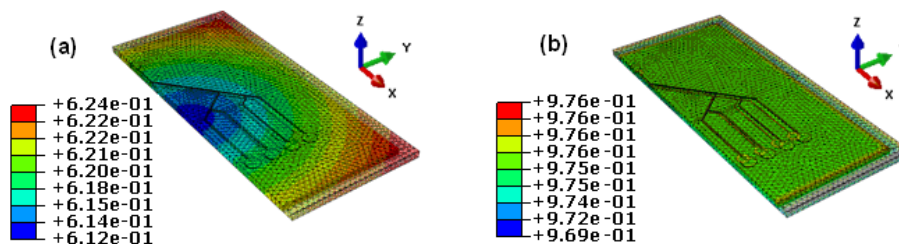


Fig. 5. Final distribution of the relative density in micro-fluidic specimens of 316L stainless steel powders, obtained after the (a) hot embossing process and (b) sintering stage at 1360°C.

The sintering process gives the sintered components a nearly uniform final density distribution in spite of the inhomogeneous green density distribution due to segregation occurring during the embossing step (see Fig. 6.). After the sintering stage, the relative densities are homogeneous for most of the simulations, in which the variations have been well controlled within 1%. Increasing the sintering temperature from 1150 °C to 1360 °C resulted in the average density increasing from 6.16 g/cm<sup>3</sup> to 7.66 g/cm<sup>3</sup>. In addition to the relative densities, the shrinkages were also simulated for these micro-fluidic components embossed with different conditions (see Fig. 7) presents the variation range of shrinkage during the sintering process. There is no obvious shrinkage before the temperature reaches 1050 °C, which is due to the high viscosity of the specimens at low temperatures. The maximum densification rate occurs beyond 1250 °C.

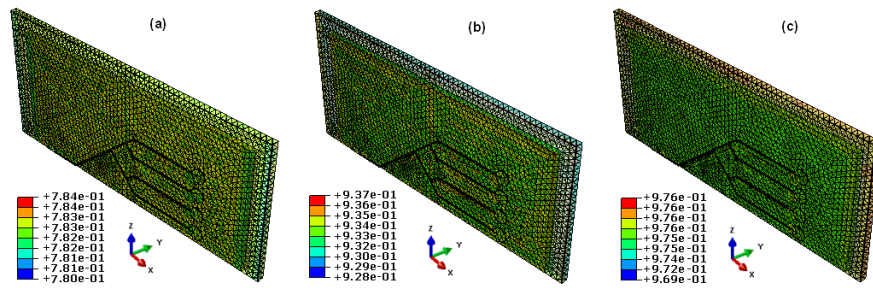


Fig. 6. Final numerical relative density of the sintered micro-fluidic components after sintering at different temperatures: (a) 1150°C, (b) 1250°C and (c) 1360°C (solid loading: 62%, heating rate: 15°C/min, hold time: 120 min).

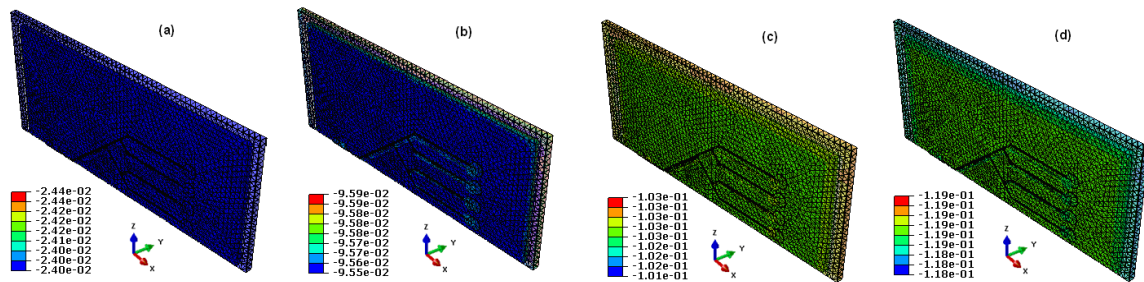


Fig. 7. Numerical final shrinkage of the sintered micro-fluidic components versus sintering temperature: (a) 1050°C, (b) 1150°C, (c) 1250°C and (d) 1360°C (heating rate, 15°C/min; solid loading of 62%).

## 5 Experimental Validation and Discussion

The microfluidics replication has been obtained by embossing process using feedstocks ranging from 60 to 64 vol%. Then the embossed samples were subjected to thermal debinding at 500 °C for 1 h and subsequently sintered in a high-vacuum furnace at 1360 °C for 2 h. The sintered samples were free of physical defects (see Fig. 8).



Fig. 8. Photographs of the micro-fluidic replicas after the: (a) embossing (b) debinding and (c) sintering steps, which were produced using 316L stainless steel feedstock (solid loading : 64%).

The relative density of the micro-fluidic specimens obtained from the numerical simulations is compared with the experimental values, as shown in Fig. 9a. The relative densities are in perfect agreement with the experimental densities, particularly for the sintering cycles with relatively low heating rates. A comparison between the experimental and the simulation results of the shrinkage in three directions (length, width and height) is shown in Fig. 9b. During the sintering stage, the simulated dimensions were in good accordance with the experimental values with a relative error of less than 3% in both directions. In addition, both the simulated and experimental shrinkages in the height direction were higher than those in the other two directions, which is primarily due to gravity along the height direction.

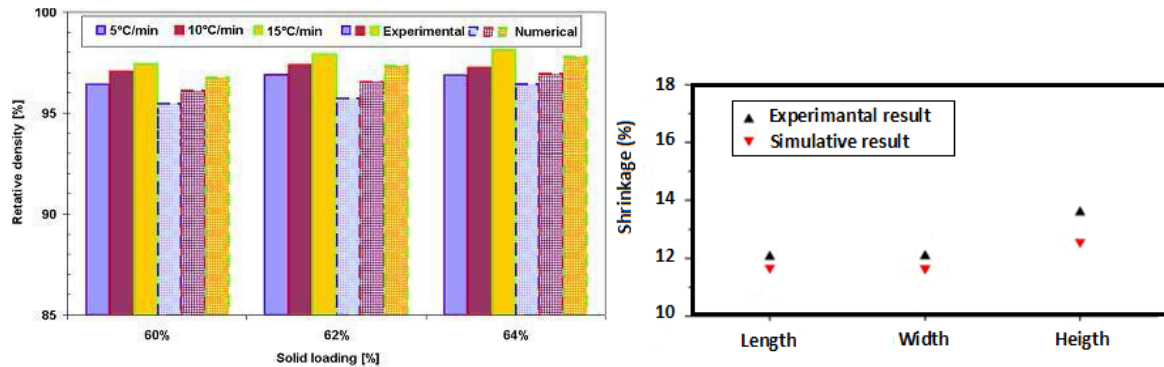


Fig. 9. Comparison between the experimental and simulated results of (a) relative density and (b) shrinkage in three directions.

## 6 Conclusions

Numerical simulations was performed to investigate the shrinkage variations and relative density evolutions during a powder hot embossing process. The effects of the heating rates, green density, solid loading and sintering temperature were investigated. The following conclusions can be made:

- The densification occurs primarily in the heating period and is extremely sensitive to the heating rates. In addition, rapid sintering is favourable for densification. The maximum shrinkage of 316L stainless steel powders is -14% at a heating rate of 15 °C/min.
- The simulation of the sintering step using a finite element method was proven as an efficient method to predict the shrinkage of micro-fluidic parts. It can also be observed that the sintering process makes the final density of the sintered bodies essentially uniform. However, the components exhibit inhomogeneous shrinkage after sintering, which ranges from 11.5% to 14%.

## References

1. J.M. Li, C. Liu, J. Peng, Effect of hot embossing process parameters on polymer flow and microchannel accuracy produced without vacuum, *Journal of Materials Processing Technology* 207 (2008) 163-171
2. H. Ou, M. Sahli, J.-C. Gelin, T. Barrière, Experimental analysis and finite element simulation of the co-sintering of bi-material components, *Powder Technology* 268 (2014) 269-278
3. M-R. Raza, A-B. Sulong, N. Muhamad, M-N. Akhtar, J. Rajabi, Effects of binder system and processing parameters on formability of porous Ti/HA composite through powder injection moulding, *Materials & Design* 87 (2015) 386-392
4. M. Sahli, J.-C. Gelin, T. Barriere, Characterisation and replication of metallic microfluidic devices using three different powders processed by hot embossing, *Powder Technology* 246 (2013) 284-302
5. Naci Kurgan, Effects of sintering atmosphere on microstructure and mechanical property of sintered powder metallurgy 316L stainless steel, *Materials & Design* 52 (2013) 995-998
6. J-P. Choi, G-Y. Lee, J-I. Song, W-S. Lee, J-S. Lee, Sintering behavior of 316L stainless steel micro-nanopowder compact fabricated by powder injection moulding, *Powder Technology* 279 (2015) 196-202
7. J. Rajabi, N. Muhamad, A-B. Sulong, A. Fayyaz, M-R. Raza, The effect of nano-sized stainless steel powder addition on mechanical and physical properties of micropowder injection molded part, *Materials & Design* 63 (2014) 223-232
8. E.A. Olevsky, Theory of sintering: from discrete to continuum, *Mater. Sci. Eng.* 23 (1998) 41-100
9. J. Song, J.C. Gelin, T. Barrière, B. Liu, Experiments and numerical modelling of solid state sintering for 316L stainless steel components, *Journal of Materials Processing Technology* 177 (2006) 352-355